


 Cite this: *RSC Adv.*, 2025, 15, 14893

# Enhanced structural and optoelectronics performance of perovskite solar cells *via* MnSe<sub>2</sub> incorporation in a MAPbI<sub>3</sub> absorber layer

 Muhammad Sikandar Farooq,<sup>a</sup> Dhafer O. Alshahrani,<sup>b</sup> Sadia Kanwal,<sup>a</sup>  
 Muhammad Umar Farooq,<sup>c</sup> Qurat Ul Ain<sup>df</sup> and Muhammad Saad<sup>ib\*ef</sup>

This study presents a novel approach for enhancing the efficiency of perovskite solar cells (PSCs) by incorporating MnSe<sub>2</sub> into a MAPbI<sub>3</sub> absorber layer. UV-visible (UV-vis) spectroscopy revealed a redshift in the absorption edge, reducing the bandgap from 1.71 eV to 1.62 eV, indicating improved light absorption. The refractive index increased from 2.84 to 2.89, while the extinction coefficient increased from 2.215 to 2.222, ensuring minimal non-radiative losses. Photoluminescence (PL) spectroscopy exhibited an enhanced emission peak, suggesting reduced non-radiative recombination. X-ray diffraction (XRD) analysis showed an increased crystallite size from 25.4 nm to 34.1 nm, with a decrease in dislocation line density (DLD) from  $1.55 \times 10^{15}$  to  $0.86 \times 10^{15}$ , indicating improved crystallinity. Electrochemical impedance spectroscopy (EIS) revealed an increase in recombination resistance ( $R_{rec}$ ) from 4835  $\Omega$  to 5941  $\Omega$ , confirming reduced charge recombination. Current density–voltage ( $J$ – $V$ ) measurements demonstrated an increase in power conversion efficiency (PCE) from 18.09% (MAPbI<sub>3</sub>) to 21.95% (MnSe<sub>2</sub>–MAPbI<sub>3</sub>), attributed to enhanced charge transport and energy band modification. External quantum efficiency (EQE) measurements further validated the improved light-harvesting capability of MnSe<sub>2</sub>–MAPbI<sub>3</sub>. These findings highlight MnSe<sub>2</sub> as a promising additive for high-performance PSCs, offering improved optical, structural, and photovoltaic properties. Future research can explore stability enhancement for long-term device performance.

 Received 1st April 2025  
 Accepted 2nd May 2025

DOI: 10.1039/d5ra02254a

[rsc.li/rsc-advances](https://rsc.li/rsc-advances)

## 1. Introduction

The expanding energy problem, which is being brought on by the depletion of fossil fuel reserves and rising global energy use, has raised the need for sustainable and renewable energy sources.<sup>1</sup> The quantity of solar energy and its benefits for the environment have made it a viable alternative.<sup>2</sup> In particular, photovoltaic (PV) technology has made tremendous strides, and perovskite solar cells (PSCs) have shown remarkable potential due to their high efficiency and low production costs.<sup>3</sup> The improved stability and environmental robustness of inorganic PSCs have made them attractive substitutes for organic and hybrid perovskites. For application in solar cells, a variety of inorganic perovskite compositions, such as CsPbI<sub>3</sub>, CsPbBr<sub>3</sub>,

and CsSnI<sub>3</sub>, have been studied.<sup>4</sup> Nonetheless, methylammonium lead iodide (MAPbI<sub>3</sub>) continues to be the most studied perovskite because of its remarkable optoelectronic characteristics, which include a long charge carrier diffusion length, a high absorption coefficient, and an adjustable bandgap ( $\sim 1.75$  eV).<sup>5</sup> PSCs based on MAPbI<sub>3</sub> are comparable to traditional silicon-based solar cells due to their high power conversion efficiencies (PCEs).<sup>6</sup> Despite these advantages, MAPbI<sub>3</sub> vulnerability to moisture and heat instability causes stability issues under ambient conditions.<sup>7,8</sup> To try to reduce these limitations, researchers have employed strategies including compositional engineering, surface passivation, doping, and encapsulation. MoSe<sub>2</sub> was added to MAPbI<sub>3</sub> perovskite by Ahmad *et al.*, who claimed that this increased device stability by up to 85%.<sup>8</sup> Maqsood *et al.* looked at how adding FA to MAPbI<sub>3</sub> increased device stability and efficiency by up to 22.02%.<sup>9</sup> Black phosphorous was added to MAPbI<sub>3</sub>, increasing the electron and hole charge carrier's diffusion life-span, according to Liu *et al.*<sup>10</sup> The focus of recent developments is on material advances to increase energy devices' stability and efficiency. Lattice engineering and multicomponent doping have produced high-entropy titanates with exceptional mechanical and thermal characteristics.<sup>11</sup> Bi-interfacial modification techniques employing fluoropyridinic acid for better

<sup>a</sup>Department of Physics, University of Sahiwal, Sahiwal, 57000, Pakistan

<sup>b</sup>Department of Physics, College of Science, University of Bisha, P.O. Box 551, Bisha 61922, Saudi Arabia

<sup>c</sup>Department of Chemistry, Bahauddin Zakariya University, Multan, 60800, Punjab, Pakistan

<sup>d</sup>Department of Physics, University of Education, Lahore, Punjab, Pakistan

<sup>e</sup>Department of Electrical Engineering, COMSATS University Islamabad, Lahore Campus, Lahore, Punjab, Pakistan. E-mail: msaad.edu.comsats@gmail.com

<sup>f</sup>Department of Physics, Punjab Group of Colleges, Lahore, Punjab, Pakistan


defect passivation in PSCs and controlled etching for silicon recycling, also demonstrate new avenues for producing long-lasting and high-performing solar cells.<sup>12,13</sup>

Among the various approaches to enhance the stability and efficiency of MAPbI<sub>3</sub> PSCs, doping and additive strategies have emerged as effective methods. Doping elements like alkali metals, transition metals, and halides into the perovskite structure can improve charge transport properties and reduce trap states.<sup>14</sup> Electron transport layers (ETLs) such as TiO<sub>2</sub>, SnO<sub>2</sub>, and ZnO have also been optimized to improve charge extraction and device stability.<sup>15</sup> Furthermore, additive strategies incorporating materials like 2D perovskites, quantum dots, and metal chalcogenides have shown promise in enhancing the performance of MAPbI<sub>3</sub> PSCs. These strategies address critical issues such as non-radiative recombination, defect passivation, and moisture resistance, leading to improved device efficiency and operational stability.<sup>16,17</sup>

Manganese selenide (MnSe<sub>2</sub>) has garnered interest because of its exceptional visual qualities, high carrier mobility, and distinct electrical structure.<sup>18</sup> However, because of its comparatively worse stability and less-than-ideal band alignment for effective charge extraction, its independent use in photovoltaics has been restricted.<sup>18</sup> Various researcher has studied the transition metals (Mn, Mo *etc.*) di-selenide-based materials for different application. The advantageous use of Cu-doped MnSe<sub>2</sub> for the creation of hydrogen was documented by Soni *et al.*<sup>19</sup> The Sm-doped MoSe<sub>2</sub> ETL employed to improve the PCE for lead-based PSCs by Anandh *et al.*<sup>20</sup> The potential of the MnSe<sub>2</sub> electrode for use in supercapacitors was investigated by Phatak *et al.*<sup>21</sup> Thus, the various researchers reported the MnSe<sub>2</sub> application in the different field, but the performance of MnSe<sub>2</sub> based material in the field of solar cell is still under investigation. MnSe<sub>2</sub> can be added to MAPbI<sub>3</sub> perovskite films to improve charge transport characteristics, passivate faults, and increase stability. The inherent drawbacks of MAPbI<sub>3</sub> can be addressed by adding MnSe<sub>2</sub>, which can decrease trap states, inhibit non-radiative recombination, and increase carrier lifetime.<sup>22,23</sup> Additionally, by partially replacing Pb with Mn, MnSe<sub>2</sub>-MAPbI<sub>3</sub> composites can have a synergistic impact that improves the structural and optoelectronic characteristics of the perovskite layer while simultaneously lowering lead toxicity. This approach is in line with current research initiatives to create lead-free or lead-reduced PSCs with improved performance and environmental compatibility.<sup>22,23</sup>

This study introduces a novel approach to improving MAPbI<sub>3</sub>-based PSCs by incorporating MnSe<sub>2</sub> as an additive. The key novelty of this work lies in the strategic incorporation of MnSe<sub>2</sub> into MAPbI<sub>3</sub> to enhance stability, and overall photovoltaic performance. The incorporation of MnSe<sub>2</sub> into the perovskite structure is expected to improve crystallinity, reduce defect density, and enhance charge transport properties. The main findings of this study reveal that MnSe<sub>2</sub>-MAPbI<sub>3</sub> films exhibit improved optoelectronic properties, leading to enhanced power conversion efficiency (PCE) from 18.09% to 21.95%. Additionally, the EIS and EQE analyses confirm reduced recombination losses and improved charge extraction in MnSe<sub>2</sub>-doped devices. This work contributes to the ongoing advancements in

perovskite solar cell technology by presenting an effective strategy for enhancing the performance and stability of MAPbI<sub>3</sub>-based solar cells through MnSe<sub>2</sub> incorporation.

## 2. Experimental details

### 2.1. Materials required

Sol-gel spin coating was used to create the MAPbI<sub>3</sub> and 5% MnSe<sub>2</sub>-MAPbI<sub>3</sub> films, and structural, optical, and electrical characterisations were then performed.<sup>24,25</sup> High-purity materials were employed for the synthesis process, including lead iodide (PbI<sub>2</sub>, 99.99%, Sigma-Aldrich), methylammonium iodide (MAI, 99.5%, GreatCell Solar), and manganese selenide (MnSe<sub>2</sub>, 99.9%, Sigma-Aldrich). Solvents such as dimethyl sulfoxide (DMSO, ≥99.9%, Sigma-Aldrich), *N,N*-dimethylformamide (DMF, ≥99.8%, Sigma-Aldrich), and isopropanol (IPA, ≥99.9%, Sigma-Aldrich) were utilized for precursor solution preparation. Titanium dioxide (TiO<sub>2</sub>, 99.7%, Sigma-Aldrich) served as the electron transport layer (ETL), while Spiro-OMeTAD (99.8%, Sigma-Aldrich) was used as the hole transport layer (HTL). Every chemical was utilized without any additional purification.

### 2.2. Synthesis

In order to create MAPbI<sub>3</sub> films, a 1 M solution of PbI<sub>2</sub> (461 mg) and MAI (159 mg) was prepared in 1 mL of a DMF : DMSO combination (4 : 1 v/v). The mixture was then stirred for an hour at 70 °C to produce a uniform yellow solution. MnSe<sub>2</sub> nanoparticles, which were initially dispersed in DMF : DMSO and sonicated for 30 minutes before mixing with PbI<sub>2</sub> and MAI, were used in place of 5 mol% of PbI<sub>2</sub> for the 5% MnSe<sub>2</sub>-MAPbI<sub>3</sub> films.<sup>8</sup> The same conditions were then used to agitate the solution. To improve surface wettability, FTO-coated glass substrates were ultrasonically cleaned for 15 minutes each in acetone, ethanol, and isopropanol. This was followed by a 10-minute oxygen plasma treatment. A two-step spin coating procedure was used to deposit the films on FTO: 1000 rpm for 10 s was used to distribute the solution, and then 4000 rpm for 30 s was used. After 10 seconds, 300 μL of toluene was dropped to help crystallise the film. To finish the perovskite conversion, the films were then annealed for 15 minutes at 100 °C within a glove box (O<sub>2</sub> < 0.1 ppm, H<sub>2</sub>O < 0.1 ppm).<sup>8</sup>

### 2.3. Characterization

Tauc's relation was used to compute the optical bandgap ( $E_g$ ), and Shimadzu UV-2600 UV-vis spectroscopy was used to analyze the films' optical properties.<sup>26</sup>

$$\alpha hv = A(hv - E_g)^n \quad (1)$$

where,  $\alpha = \frac{2.303A}{d}$ , for direct bandgap semiconductors,  $n = 2$ ,  $d$  is the film thickness,  $\alpha$  is the absorption coefficient,  $hv$  is the photon energy, and  $A$  is a constant. To assess charge carrier recombination, the photoluminescence (PL) spectra were recorded using a Horiba FluoroMax-4. The structural characteristics were analyzed using X-ray diffraction (XRD, PANalytical



X'Pert Pro) with a Cu-K $\alpha$  ( $\lambda = 1.5406 \text{ \AA}$ ) source. Scherrer's eqn (2) was used to determine the crystallite size ( $D$ ), while eqn (3) and (4) were used to determine the dislocation density (DL), the lattice constant ( $a$ ), and Bragg's law was used to estimate the interplanar spacing ( $d$ ), as shown in eqn (5) below:<sup>27,28</sup>

$$D = \frac{K\lambda}{\beta \cos \theta} \quad (2)$$

$$\text{DL} = \frac{1}{D^2} \quad (3)$$

$$d = \frac{n\lambda}{2 \sin \theta} \quad (4)$$

$$a_{\text{exp}} = d\sqrt{h^2 + k^2 + l^2} \quad (5)$$

where the Miller indices are ( $h, k, l$ ),  $K$  is 0.9,  $\theta$  is the X-ray wavelength,  $\beta$  is the full-width at half maximum (FWHM), and  $\theta$  is the Bragg angle. The perovskite solar cell (PSC) devices were fabricated in the structure FTO/TiO<sub>2</sub>/MAPbI<sub>3</sub>/Spiro-OMeTAD/Au and FTO/TiO<sub>2</sub>/MnSe<sub>2</sub>-MAPbI<sub>3</sub>/Spiro-OMeTAD/Au to evaluate photovoltaic performance. A Keithley 2400 Source Meter was used to assess  $J$ - $V$  characteristics in an AM 1.5G illumination setting (100 mW cm<sup>-2</sup>, Newport Solar Simulator). The fill factor (FF) and power conversion efficiency (PCE) were calculated using the following formulae:<sup>29</sup>

$$\text{FF} = \frac{P_{\text{max}}}{J_{\text{sc}} \times V_{\text{oc}}} \quad (6)$$

$$\eta = \frac{V_{\text{oc}} \times J_{\text{sc}} \times \text{FF}}{P_{\text{in}}} \quad (7)$$

where  $J_{\text{sc}}$  is the short-circuit current density,  $V_{\text{oc}}$  is the open-circuit voltage, FF is the fill factor, and  $P_{\text{in}}$  is the incident power. An Autolab PGSTAT302N was used for EIS between 1 Hz and 1 MHz in order to extract characteristics like recombination resistance ( $R_{\text{rec}}$ ) and charge transfer resistance ( $R_{\text{ct}}$ ). A Newport Oriol IQE-200 was used to measure the EQE spectra in order to assess the wavelength-dependent photocurrent response.

## 3. Results and discussion

### 3.1. UV-vis spectroscopy

The UV-vis absorption spectra of 0%, 4%, 5%, and 6% MnSe<sub>2</sub>-incorporated MAPbI<sub>3</sub> films are shown in Fig. 1a. All the prepared perovskite films show extensive absorption in the visible spectrum. Interestingly, the absorption edge changes when MnSe<sub>2</sub> is added. The pure MAPbI<sub>3</sub> film exhibits an excitonic absorption start at 725 nm. While 4%, and 5% MnSe<sub>2</sub>-MAPbI<sub>3</sub> films display redshifts to 737 nm and 742 nm, followed by a minor blueshift to 723 nm for 6% MnSe<sub>2</sub>. Better orbital overlap and lower bandgap transitions are made possible by increased crystallinity and decreased defect density, which are the reasons for the redshift up to 5% MnSe<sub>2</sub>.<sup>30,31</sup> Phase segregation, which provides localized states that impede efficient absorption, or excessive doping, which causes lattice distortion, might be the cause of the following blueshift at 6% MnSe<sub>2</sub>. In photovoltaic applications, redshifted absorption is especially

advantageous since it makes it possible to gather lower-energy photons, so expanding the useable solar spectrum. The prolonged absorption of the 5% MnSe<sub>2</sub>-MAPbI<sub>3</sub> film in this instance indicates improved photo-response, which makes it an excellent choice for an active layer in PSCs.<sup>31</sup>

Tau's plots were used to examine the optical bandgap ( $E_{\text{g}}$ ) of the films.<sup>32</sup> The calculated bandgaps for MnSe<sub>2</sub>-MAPbI<sub>3</sub> films are 1.71 eV, 1.68 eV, 1.62 eV, and 1.75 eV for 0%, 4%, 5%, and 6% MnSe<sub>2</sub>, respectively, as seen in Fig. 1b. Improved crystallinity, band tailing from mild doping, and electrical structural modulation that narrows the bandgap are the reasons for the bandgap decrease with increasing MnSe<sub>2</sub> concentration up to 5%.<sup>11-13</sup> Nevertheless, bandgap widening is seen at 6% doping, which might be brought on by non-radiative recombination centers that interfere with the charge transport channels or by too much MnSe<sub>2</sub> bringing structural disorder.<sup>33</sup> PSCs benefit from a lowered bandgap at 5% MnSe<sub>2</sub> (1.62 eV) since it closely resembles the optimal bandgap range for single-junction solar cells,<sup>34</sup> enabling improved light absorption and an elevated short-circuit current density ( $J_{\text{sc}}$ ). Accordingly, the optical analysis shows that the most advantageous optical properties for photovoltaic performance are provided by 5% MnSe<sub>2</sub> inclusion into MAPbI<sub>3</sub>. Our PSCs are made from pure MAPbI<sub>3</sub> and 5% MnSe<sub>2</sub>-MAPbI<sub>3</sub> films, which are great options for creating effective perovskite solar cells. Additionally, as illustrated in Fig. 1c, the extinction coefficient ( $K$ ) and refractive index ( $n$ ) were examined to evaluate the optical behavior of the films.<sup>35</sup> The extinction coefficient rose from 2.215 to 2.222, and the refractive index of MAPbI<sub>3</sub> was determined to be 2.84, slightly increasing to 2.89 for MnSe<sub>2</sub>-MAPbI<sub>3</sub>. This modest increase in refractive index points to improved light-trapping and optical confinement in the MnSe<sub>2</sub>-MAPbI<sub>3</sub> film, which can enhance photon recycling in the active layer and boost efficiency.<sup>36</sup> The extinction coefficient, which measures the material's capacity to absorb light, little changes, suggesting that the addition of MnSe<sub>2</sub> does not result in a significant amount of non-radiative losses. PSC performance is improved by the combined effect of a greater refractive index and a regulated extinction coefficient, which guarantee ideal optical characteristics for effective light management.<sup>37</sup>

### 3.2. PL intensity

The absorption edge shown in the UV-vis spectra is consistent with emission peaks at 729 nm and 744 nm, respectively, in the photoluminescence (PL) spectra of MAPbI<sub>3</sub> and 5% MnSe<sub>2</sub>-MAPbI<sub>3</sub> films, as illustrated in Fig. 2. The MnSe<sub>2</sub>-MAPbI<sub>3</sub> PL peak redshift indicates a decrease in the bandgap, which demonstrates that the incorporation of MnSe<sub>2</sub> has changed the electrical structure.<sup>8</sup> Defect states or band bending effects, which promote carrier relaxation to lower energy levels prior to radiative recombination, are responsible for this change.<sup>8</sup> Furthermore, effective suppression of non-radiative recombination losses is suggested by the observed rise in PL emission intensity upon insertion of MnSe<sub>2</sub>. By interacting with under-coordinated ions, MnSe<sub>2</sub> may be able to passivate surface traps and grain boundary defects, reducing recombination centers



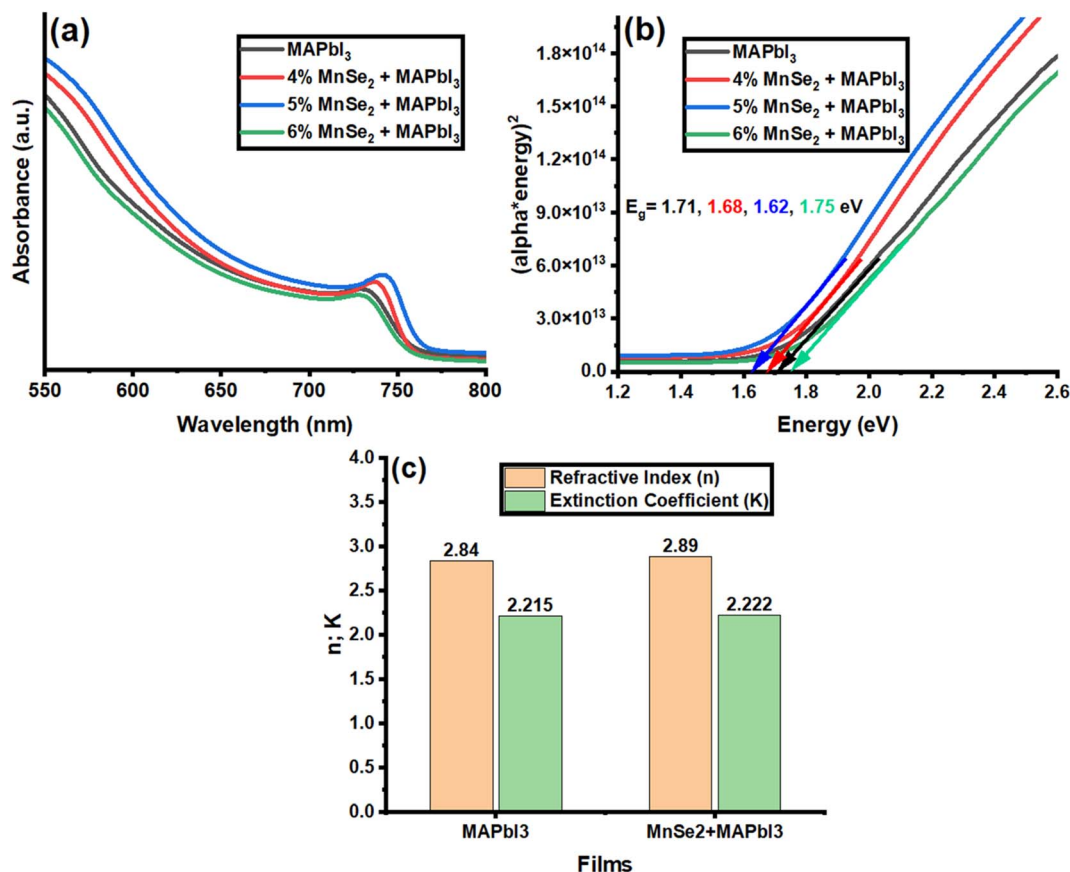


Fig. 1 (a) Absorption graph, (b) Tau\*c plots of MAPbI<sub>3</sub>, 4%, 5%, and 6% MnSe<sub>2</sub>-MAPbI<sub>3</sub>, (c) Calculated values of *n* and *K* of MAPbI<sub>3</sub> and 5% MnSe<sub>2</sub>-MAPbI<sub>3</sub>.

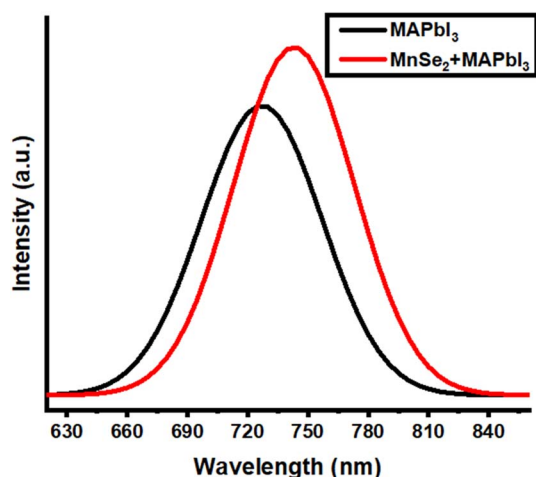


Fig. 2 PL intensity of MAPbI<sub>3</sub> and 5% MnSe<sub>2</sub>-MAPbI<sub>3</sub>.

associated with defects.<sup>38</sup> By encouraging radiative recombination processes, this passivation increases the device's overall efficiency and carrier lifetime. This result emphasizes how important MnSe<sub>2</sub> is for improving the perovskite film's optoelectronic quality.<sup>8,38</sup>

### 3.3. X-ray diffraction

An essential method for examining the crystalline quality, phase purity, and crystallographic structure of thin films is XRD. The XRD pattern of the MAPbI<sub>3</sub> films displays distinctive diffraction peaks that correspond to the (110), (220), (222), and (314) crystal planes, as illustrated in Fig. 3a. These peaks are suggestive of the tetragonal phase of MAPbI<sub>3</sub>.<sup>8,39</sup> A well-ordered crystal development within the film is confirmed by the crisp and well-defined diffraction peaks, which indicate good crystallinity. The successful production of the MAPbI<sub>3</sub> phase with high purity is further guaranteed by the lack of secondary phases or peaks associated with impurities.<sup>40</sup> By decreasing grain boundary defects, this high crystallinity significantly improves charge transport characteristics and raises the overall photovoltaic performance of perovskite solar cells (PSCs).<sup>41</sup> Additional peaks at the (111), (200), (210), and (211) diffraction planes in the 5% MnSe<sub>2</sub>-MAPbI<sub>3</sub> film's XRD pattern are ascribed to the presence of MnSe<sub>2</sub> and are in good agreement with the JCPDS card number# 65-3336, confirming the successful incorporation of MnSe<sub>2</sub> into the perovskite matrix.<sup>42</sup> No secondary phases were detected in the XRD patterns after MnSe<sub>2</sub> incorporation, confirming that MnSe<sub>2</sub> is well integrated into the perovskite matrix without disrupting the MAPbI<sub>3</sub> crystal structure. This supports the claim of enhanced crystallinity, as



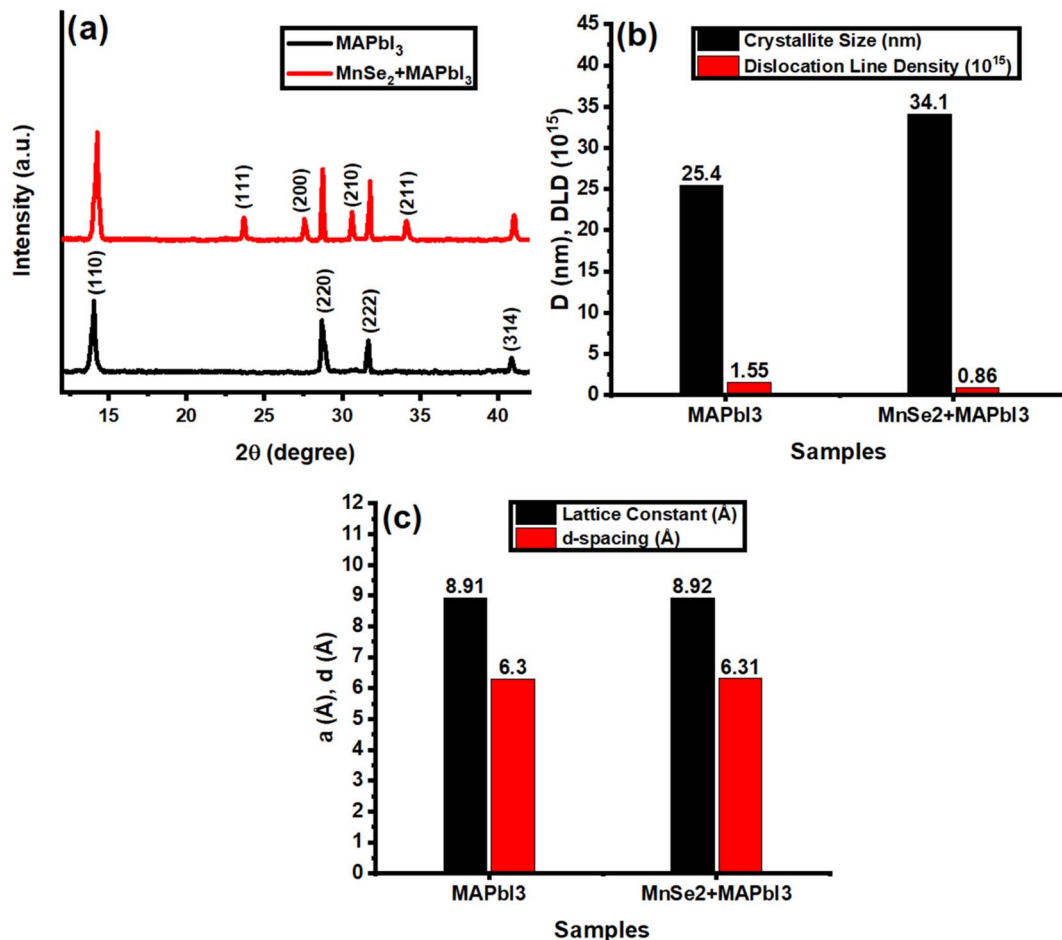


Fig. 3 (a) XRD pattern (b) calculated value of  $D$  and DLD (c) calculated values of  $a$  and  $d$ -spacing of MAPbI<sub>3</sub> and 5% MnSe<sub>2</sub>-MAPbI<sub>3</sub>.

pure and sharp diffraction peaks indicate improved film quality.<sup>43–45</sup> The MnSe<sub>2</sub> addition functions as a nucleation site, enabling better grain formation, which is responsible for the observed increase in peak intensity in 5% MnSe<sub>2</sub>-MAPbI<sub>3</sub> films when compared to pure MAPbI<sub>3</sub>.<sup>46</sup> PSCs benefit from this increase in crystallinity because it lowers defect densities, increases charge carrier mobility, and decreases non-radiative recombination, all of which improve device performance.<sup>46</sup> Using Scherrer's equation,<sup>27,28</sup> the predicted crystallite size increases from 25.4 nm in pure MAPbI<sub>3</sub> films to 34.1 nm in 5% MnSe<sub>2</sub>-MAPbI<sub>3</sub> films, suggesting that MnSe<sub>2</sub> addition improves grain growth. The improved crystalline quality of the MnSe<sub>2</sub>-based film is further supported by the dislocation line density (DLD), which is inversely correlated with crystallite size and drops from  $1.55 \times 10^{15}$  to  $0.86 \times 10^{15}$  lines per m<sup>2</sup>.<sup>47</sup> Additionally, as seen in Fig. 3c, the structural characteristics for both films, including the lattice constant and  $d$ -spacing, were computed.<sup>27,28</sup> From 8.91 Å in MAPbI<sub>3</sub> to 8.92 Å in 5% MnSe<sub>2</sub>-MAPbI<sub>3</sub>, the lattice constant increases marginally, indicating a little lattice expansion brought on by MnSe<sub>2</sub>. In line with the change in peak positions, the  $d$ -spacing also rises from 6.30 Å to 6.31 Å.<sup>27,28</sup> The slight expansion of the lattice parameter can be associated with strain relaxation effects introduced by MnSe<sub>2</sub>

incorporation, which aids in reducing defect states and improving film stability. This structural modification is advantageous for PSCs as it facilitates better charge transport, reduces defect-mediated recombination, and enhances light absorption, ultimately leading to improved power conversion efficiency.<sup>47</sup>

### 3.4. Device performance

As schematic diagram shown in Fig. 4a, two perovskite solar cell (PSC) devices were fabricated with the following configurations to examine the effect of the produced films as an active absorber layer such as device-1 (FTO/TiO<sub>2</sub>/MAPbI<sub>3</sub>/Spiro-OMeTAD/Au) and device-2 (FTO/TiO<sub>2</sub>/5%MnSe<sub>2</sub>-MAPbI<sub>3</sub>/Spiro-OMeTAD/Au). The absorption of photons by the perovskite active layer causes the creation of electron-hole pairs, in which holes migrate toward the hole transport layer (HTL) and electrons travel toward the electron transport layer (ETL).<sup>48</sup> The ETL in the device construction is TiO<sub>2</sub>, which minimizes recombination losses by removing photogenerated electrons from the perovskite layer and transferring them toward the FTO electrode while obstructing hole transit.<sup>48</sup> The light-absorbing substance that generates charge carriers is the perovskite layer (MAPbI<sub>3</sub> or MnSe<sub>2</sub>-MAPbI<sub>3</sub>). In order to provide effective charge separation



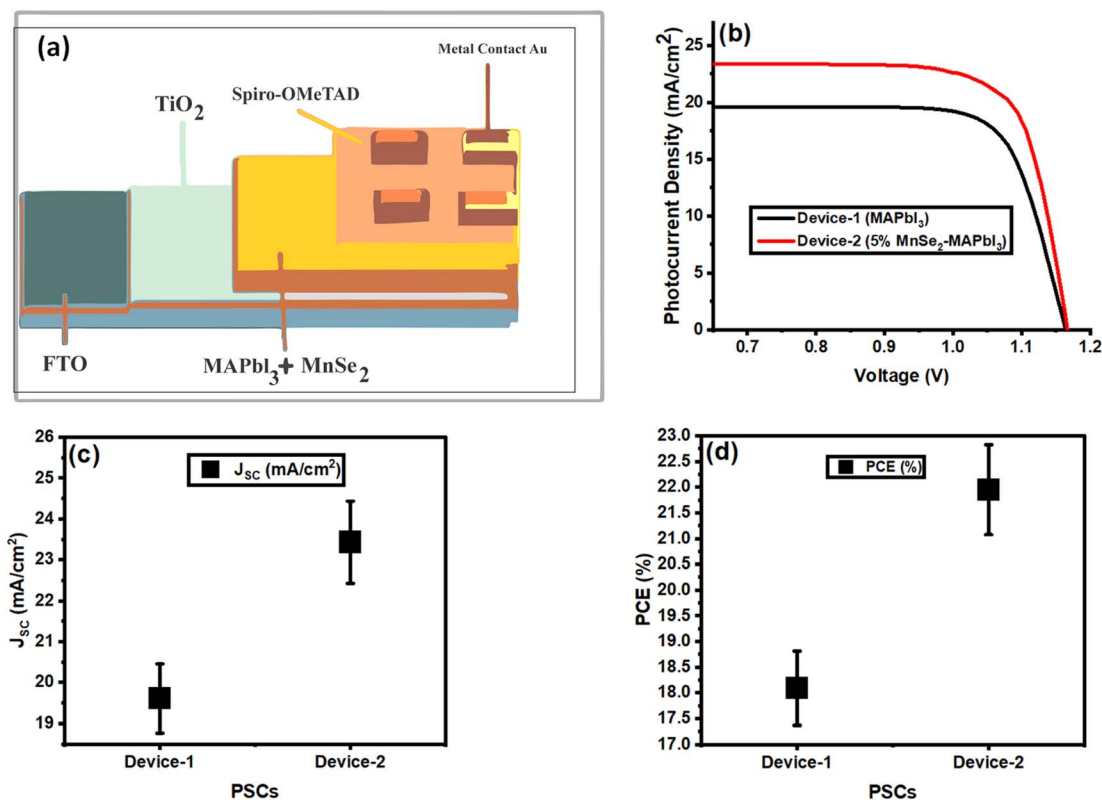


Fig. 4 (a) Schematic diagram of PSC (b)  $J$ - $V$  measurement (c) calculated values of  $J_{sc}$  ( $\text{mA cm}^{-2}$ ) (d) calculated values of PCE (%) of device-1 ( $\text{MAPbI}_3$  based) and device-2 ( $\text{MnSe}_2$ - $\text{MAPbI}_3$  based) PSCs.

and transport within the device, the Spiro-OMeTAD serves as the HTL, gathering photogenerated holes from the perovskite layer and moving them in the direction of the Au electrode.<sup>48</sup>

**3.4.1.  $J$ - $V$  measurement.** Fig. 4b shows the  $J$ - $V$  characteristics of the two fabricated PSCs, demonstrating a notable improvement in performance for device-2 (5%  $\text{MnSe}_2$ - $\text{MAPbI}_3$ -based). Table 1 presents the averaged photovoltaic parameters derived from  $J$ - $V$  measurements of ten devices each for  $\text{MAPbI}_3$  and 5%  $\text{MnSe}_2$ - $\text{MAPbI}_3$ , confirming the enhanced performance with  $\text{MnSe}_2$  incorporation. As summarized in Fig. 4(c) and (d), device-1 ( $\text{MAPbI}_3$ -based) has a short-circuit current density ( $J_{sc}$ ) of  $19.61 \text{ mA cm}^{-2}$ , an open-circuit voltage ( $V_{oc}$ ) of  $1.162 \text{ V}$ , a fill factor (FF) of  $0.794$ , and a power conversion efficiency (PCE) of  $18.09\%$ . The device-2 (5%  $\text{MnSe}_2$ - $\text{MAPbI}_3$ ), on the other hand, shows better values with  $J_{sc} = 23.43 \text{ mA cm}^{-2}$ ,  $V_{oc} = 1.168 \text{ V}$ , FF =  $0.802$ , and PCE =  $21.95\%$ . The addition of  $\text{MnSe}_2$ , which efficiently alters the perovskite layer, lowering its energy bandgap and enhancing charge carrier dynamics, is responsible

for the improvement in FF and PCE.<sup>49</sup> Furthermore, improved electron injection into  $\text{TiO}_2$  is made possible by the conduction band alignment between  $\text{TiO}_2$  and  $\text{MnSe}_2$ - $\text{MAPbI}_3$ , which lowers recombination losses. Because of the enhanced charge extraction and decreased recombination, device-2 (5%  $\text{MnSe}_2$ - $\text{MAPbI}_3$ ) performs better overall, making  $\text{MnSe}_2$ - $\text{MAPbI}_3$  a viable option for high-efficiency PSCs. Improvements in short-circuit current density ( $J_{sc}$ ), fill factor (FF), and open-circuit voltage ( $V_{oc}$ ) are the main causes of the increase in PCE from  $18.09\%$  to  $21.95\%$ . Better charge carrier extraction and reduced recombination losses lead to enhanced  $J_{sc}$  and FF. Furthermore, reduced non-radiative recombination pathways are reflected in the elevated  $V_{oc}$ .<sup>49,50</sup>

**3.4.2. EQE spectra.** The External Quantum Efficiency (EQE) spectra of devices-1 ( $\text{MAPbI}_3$ ) and device-2 (5%  $\text{MnSe}_2$ - $\text{MAPbI}_3$ ) are shown in Fig. 5a. In line with the absorption profile of  $\text{MAPbI}_3$  perovskite materials, both devices show a robust photo response throughout a wide wavelength range of  $300 \text{ nm}$  to

Table 1 Calculated photovoltaic parameters of 10, 10 devices-based on the perovskite ( $\text{MAPbI}_3$  and 5%  $\text{MnSe}$ - $\text{MAPbI}_3$ ) from the  $J$ - $V$  measurement

PSCs	$V_{oc}$ (V) $\pm 0.001$	$J_{sc}$ ( $\text{mA cm}^{-2}$ ) $\pm 0.0043$	FF $\pm 0.002$	Efficiency (%) $\pm 0.004$
Pure $\text{MAPbI}_3$	1.162	19.61	0.794	18.09
5% $\text{MnSe}_2$ - $\text{MAPbI}_3$	1.168	23.43	0.802	21.95



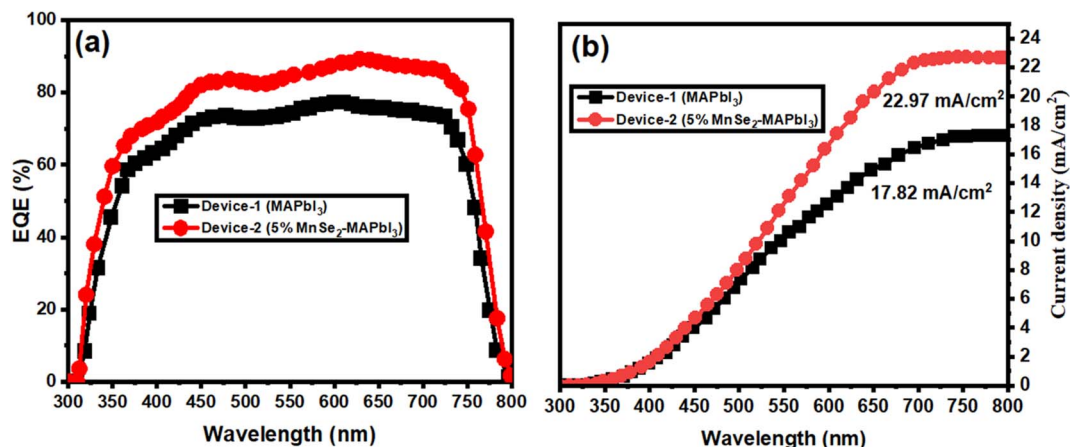


Fig. 5 (a and b) EQE spectra with corresponding  $J_{sc}$  of device-1 (MAPbI<sub>3</sub> based) and device-2 (5% MnSe<sub>2</sub>-MAPbI<sub>3</sub> based) PSCs.

800 nm. Interestingly, device-2 (5% MnSe<sub>2</sub>-MAPbI<sub>3</sub>) has a substantially greater EQE throughout the spectrum than device-1, especially in the 400–750 nm range. The addition of MnSe<sub>2</sub>, which improves interface quality and lowers charge recombination, is probably the cause of this improvement, which indicates better photon absorption and more effective charge carrier creation and extraction in device-2 (5% MnSe<sub>2</sub>-MAPbI<sub>3</sub>).<sup>9</sup> Fig. 5b shows the integrated  $J_{sc}$  values that correlate to the EQE spectra. According to the EQE curves trend, device-1 (MAPbI<sub>3</sub>) attains an integrated  $J_{sc}$  of 17.82 mA cm<sup>-2</sup>, whereas device-2 gets a higher value of 22.97 mA cm<sup>-2</sup>. Better total photovoltaic performance is achieved by device-2 improved  $J_{sc}$ , which represents its increased light-harvesting efficiency and greater charge collecting qualities. Importantly, the  $J_{sc}$  values derived from EQE integration are marginally lower than the  $J-V$  curve measurements for both devices.<sup>10</sup> The fact that EQE tests are usually carried out using a low-intensity monochromatic light source, which could not completely activate all photo-physical processes within the device, provides a scientific reason for this disparity. High-intensity, broad-spectrum AM 1.5G illumination, on the other hand, is used for  $J-V$  measurements. In this setting, increased photon flux can result in greater trap state filling, light-induced defect passivation, and better carrier mobility, all of which can raise  $J_{sc}$  values somewhat.<sup>9,10,51</sup>

**3.4.3. EIS spectra.** A potential method for examining charge transfer and recombination processes in PSCs is EIS. Recombination resistance ( $R_{rec}$ ), or the device's resistance to charge carrier recombination, is one of the important characteristics taken from EIS.<sup>9</sup> Better charge extraction and reduced recombination losses are indicated by a higher  $R_{rec}$  value, which enhances device performance. Device-1 and device-2 both have Nyquist plots in Fig. 6. The EIS measurements of PSCs were performed under dark conditions using a 10 mV AC perturbation around the maximum power point (MPP) bias voltage. EIS measurements were performed under dark conditions at the maximum power point (MPP) voltage to investigate intrinsic device impedance behavior.<sup>52</sup> Under illumination, increased carrier generation could alter recombination dynamics and

interface resistance, potentially leading to different impedance profiles.<sup>52</sup> The frequency range was set from 1 MHz to 1 Hz. As shown in the inset of Fig. 6, a ( $R(CR)$ ) equivalent Randles circuit model was used to fit the data with the help of ZSim software, in order to examine the EIS spectra.<sup>51</sup> This circuit is consisting a component of a chemical capacitance ( $C$ ), a recombination resistance ( $R_{rec}$ ), and a series resistance ( $R_s$ ) linked in series. Fig. 6 provides a summary of the fitted parameters. For both devices, the fitting value of  $R_s$  was found to be 18  $\Omega$ , demonstrating low wire and contact resistance.<sup>9</sup> It was discovered that device-1 (MAPbI<sub>3</sub>) recombination resistance ( $R_{rec-1}$ ) was 4835  $\Omega$ , but device-2 recombination resistance ( $R_{rec-2}$ ) was 5941  $\Omega$ . Device-2 (5% MnSe<sub>2</sub>-MAPbI<sub>3</sub>) greater photovoltaic performance is compatible with a higher  $R_{rec}$  value, which indicates suppressed charge recombination. These findings suggest that device-2 superior charge transport characteristics and interface quality result in increased device stability and efficiency.<sup>51</sup>

The operational stability of devices 1 and 2 during 250 hours under ambient settings is shown in Fig. 7. Device-1 (MAPbI<sub>3</sub>)

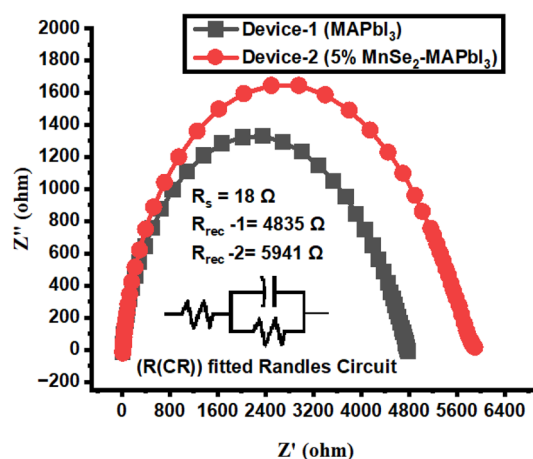


Fig. 6 EIS spectra of device-1 (MAPbI<sub>3</sub> based) and device-2 (5% MnSe<sub>2</sub>-MAPbI<sub>3</sub> based) PSCs with the inset ( $R(CR)$ ) fitted circuit by ZSim software.



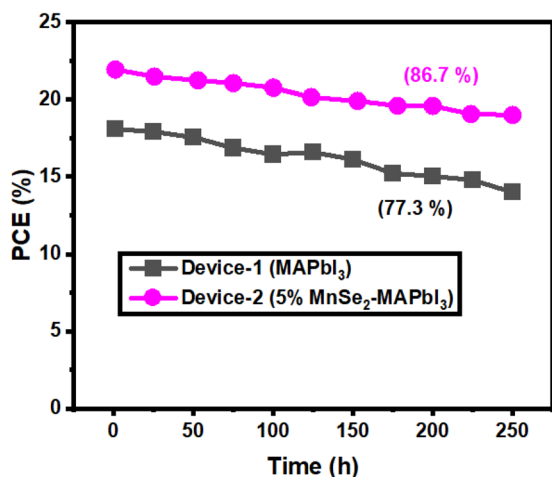


Fig. 7 Stability test over 250 hours of device-1 (MAPbI<sub>3</sub> based) and device-2 (5% MnSe<sub>2</sub>-MAPbI<sub>3</sub>) based PSCs.

barely kept 77.3% of its initial PCE, whereas device-2 (5% MnSe<sub>2</sub>-MAPbI<sub>3</sub>) kept 86.7%. The incorporation of MnSe<sub>2</sub>, which improves structural integrity and inhibits defect-induced degradation pathways, is responsible for device-2 (5% MnSe<sub>2</sub>-MAPbI<sub>3</sub>) better stability.<sup>53</sup> Device-2 (5% MnSe<sub>2</sub>-MAPbI<sub>3</sub>) shorter PCE degradation suggests less ion migration and improved moisture resistance. Furthermore, MnSe<sub>2</sub> passivation action may reduce trap states, extending the device's lifespan. These results demonstrate that MnSe<sub>2</sub> not only improves PSCs initial performance but also considerably extends their operating stability.<sup>53</sup> Thus, incorporating MnSe<sub>2</sub> into MAPbI<sub>3</sub> offers two advantages over conventional additives: improved electrical interaction with TiO<sub>2</sub> and efficient defect passivation. Better energy level alignment is made possible by MnSe<sub>2</sub> layered structure, which speeds up electron transmission and lowers recombination losses. Improved device stability and photovoltaic performance are the outcomes of this synergistic interaction. MnSe<sub>2</sub> is a very interesting addition for next-generation PSCs because of its multifunctionality.<sup>53</sup>

## 4. Conclusions

This study demonstrates the enhancement of PSCs by incorporating MnSe<sub>2</sub> into the MAPbI<sub>3</sub> absorber layer. UV-vis spectroscopy revealed a redshift in the absorption edge, reducing the  $E_g$  from 1.71 eV to 1.62 eV, indicating improved light absorption. PL spectroscopy showed increased emission intensity, confirming reduced non-radiative recombination. XRD analysis indicated improved crystallinity, with an increased crystallite size from 25.4 nm to 34.1 nm and a decreased DLD. EIS analysis revealed increased  $R_{rec}$ , confirming suppressed charge recombination.  $J-V$  measurements demonstrated an increase in PCE from 18.09% to 21.95%, attributed to enhanced charge transport and bandgap modulation. EQE analysis confirmed improved photon harvesting. These findings establish 5% MnSe<sub>2</sub>-MAPbI<sub>3</sub> as a promising candidate for high-performance PSCs with superior optical,

structural, and photovoltaic properties. Although the incorporation of MnSe<sub>2</sub> significantly improved device performance, a comprehensive defect density analysis and charge carrier mobility measurements are still needed. These studies could provide deeper insight into the intrinsic material properties and charge dynamics. Future work will focus on these aspects to further substantiate the current findings.

## Data availability

The data supporting the findings of this study will be made available upon reasonable request from the corresponding author, Muhammad Saad (msaad.comsats.edu@gmail.com).

## Conflicts of interest

All the authors in this study, have no any type of conflict of interest.

## Acknowledgements

The authors are thankful to the Deanship of Graduate Studies and Scientific Research at University of Bisha for supporting this work through the Fast-Track Research Support Program.

## References

- 1 T. Seyisi, *et al.*, Major challenges for commercialization of perovskite solar cells: A critical review, *Energy Rep.*, 2025, **13**, 1400–1415.
- 2 Z. Xingyu, Key Technologies for the Application of Perovskite Solar Cell Materials Under Energy Transition, in *The Proceedings of 2024 International Conference of Electrical, Electronic and Networked Energy Systems: Volume VIII*, Springer Nature, 2025.
- 3 L. Tariq, *et al.*, Enlightening the hydrostatic pressure variation effect on physical properties of mechanically stable La<sub>2</sub>Ge<sub>2</sub>O<sub>7</sub> pyrochlore oxide: Insights from first principles for solar cell advancement, *Phys. B*, 2025, **697**, 416698.
- 4 R. Tsuji, *et al.*, Hysteresis in Carbon-Based Multiporous Layered Electrode Perovskite Solar Cells with 5-AVA-MAPbI<sub>3</sub> and CsFAPbI<sub>3</sub>, *ACS Energy Lett.*, 2025, **10**, 1275–1283.
- 5 K. Zagorovskaia, *et al.*, Improved Operational Lifetime of MAPbI<sub>3</sub> Solar Cells Encapsulated with Parylene-N, *Sol. RRL*, 2025, 2400833.
- 6 J. V. Patil, S. S. Mali and C. K. Hong, Exceeding 23% Efficiency for 3D/3D Bilayer Perovskite Heterojunction MAPbI<sub>3</sub>/FAPbI<sub>3</sub>-Based Hybrid Perovskite Solar Cells with Enhanced Stability, *Adv. Funct. Mater.*, 2025, **35**(1), 2408721.
- 7 P. Tipparak, *et al.*, The Impact of MAPbI<sub>3</sub> Quantum Dots on CsFA Perovskite Solar Cells: Interface and Hole Extraction Improvement, *ACS Appl. Energy Mater.*, 2025, **8**(1), 355–365.
- 8 K. Ahmad, *et al.*, Fabrication of lead halide perovskite solar cells with improved photovoltaic performance using MoSe<sub>2</sub> additive strategies, *Opt. Mater.*, 2024, **157**, 116382.



- 9 A. Maqsood, *et al.*, Perovskite solar cells based on compact, smooth FA 0.1 MA 0.9 PbI<sub>3</sub> film with efficiency exceeding 22%, *Nanoscale Res. Lett.*, 2020, **15**, 1–9.
- 10 R. Liu, *et al.*, Optimizing Black Phosphorus/Halide Perovskite Compositions by Scanning Photoelectrochemical Microscopy, *J. Electrochem. Soc.*, 2022, **169**(9), 096510.
- 11 C. Gao, *et al.*, Novel high-entropy perovskite titanate: a potential thermal protective material with improved thermophysical properties, *J. Eur. Ceram. Soc.*, 2025, **45**(2), 116878.
- 12 K. Li, *et al.*, Self-Induced Bi-interfacial Modification via Fluoropyridinic Acid For High-Performance Inverted Perovskite Solar Cells, *Adv. Energy Mater.*, 2025, **15**(11), 2404335.
- 13 F. Chen, *et al.*, Short process recovery of silver and purification mechanism of crystalline silicon deep etching from end-of-life photovoltaic cells, *Chem. Eng. J.*, 2025, **510**, 161651.
- 14 Y. Yuan, *et al.*, Enhanced Spontaneous Emission Rate and Luminescence Intensity of CsPbBr<sub>3</sub> Quantum Dots Using a High-Q Microdisk Cavity, *J. Phys. Chem. Lett.*, 2025, **16**, 1095–1102.
- 15 S.-Y. Zhang, *et al.*, Optimizing ETL/CsPbBr<sub>3</sub> buried interface contact for enhanced efficiency and stability of inorganic perovskite solar cells, *Rare Met.*, 2025, 1–11.
- 16 T. Wu, *et al.*, Chlorine capped SnO<sub>2</sub> quantum-dots modified TiO<sub>2</sub> electron selective layer to enhance the performance of planar perovskite solar cells, *Sci. Bull.*, 2019, **64**(8), 547–552.
- 17 J.-B. Wu, C. Zhen and G. Liu, Photo-assisted Cl doping of SnO<sub>2</sub> electron transport layer for hysteresis-less perovskite solar cells with enhanced efficiency, *Rare Met.*, 2022, **41**, 361–367.
- 18 K. Yang, *et al.*, Hollow nanocubes of MnSe<sub>2</sub>@Cu<sub>3</sub>Se<sub>2</sub>/Cu<sub>2</sub>Se with heterostructure for ultrahigh-rate sodium storage, *Chem. Eng. J.*, 2025, 160419.
- 19 A. Soni, Development of novel CuMnSe<sub>2</sub>/ppy hybrid structure for enhancing OER electrocatalytic activity in basic environment, *J. Environ. Chem. Eng.*, 2025, **13**(3), 116690.
- 20 B. Anandh, *et al.*, Enhanced photovoltaic performance of SmMoSe<sub>2</sub> electron transport layer for perovskite solar cells, *J. Mater. Sci.: Mater. Electron.*, 2025, **36**(3), 1–20.
- 21 M. Pathak, *et al.*, A comparative experimental and theoretical investigation on energy storage performance of CoSe<sub>2</sub>, NiSe<sub>2</sub> and MnSe<sub>2</sub> nanostructures, *Appl. Mater. Today*, 2020, **19**, 100568.
- 22 M. Hussain, *et al.*, Facile fabrication of FeSe/MnSe composite for improved electrochemical characterization by hydrothermal route, *J. Electroanal. Chem.*, 2025, **976**, 118787.
- 23 X. Liu, *et al.*, Hydrothermal synthesis of cubic MnSe<sub>2</sub> and octahedral  $\alpha$ -MnSe microcrystals, *J. Cryst. Growth*, 2009, **311**(5), 1359–1363.
- 24 M. Sadaqat, *et al.*, Mn-based hierarchical polyhedral 2D/3D nanostructures MnX<sub>2</sub> (X= S, Se, Te) derived from Mn-based metal-organic frameworks as high-performance electrocatalysts for the oxygen evolution reaction, *Energy Fuels*, 2022, **36**(17), 10327–10338.
- 25 A. M. Babeer, Electronic and optoelectronic characteristics of Al/MnSe<sub>2</sub>/p-Si/Al diode, *J. Mol. Struct.*, 2021, **1245**, 131047.
- 26 P. R. Jubu, *et al.*, Considerations about the determination of optical bandgap from diffuse reflectance spectroscopy using the Tauc plot, *J. Opt.*, 2024, 1–11.
- 27 C. Humphreys, The significance of Bragg's law in electron diffraction and microscopy, and Bragg's second law, *Found. Crystallogr.*, 2013, **69**(1), 45–50.
- 28 A. Bokuniaeva and A. Vorokh, Estimation of particle size using the Debye equation and the Scherrer formula for polyphasic TiO<sub>2</sub> powder, *J. Phys. Conf. Ser.*, 2019, **1410**(1), 012057.
- 29 J. Wang, *et al.*, Charge accumulation induced S-shape J-V curves in bilayer heterojunction organic solar cells, *Org. Electron.*, 2011, **12**(6), 880–885.
- 30 M. Li, *et al.*, An ultrafast optical sensor for simultaneous detection of NH<sub>3</sub> temperature and concentration based on ultraviolet absorption spectral redshift combined with spectral reconstruction, *Sens. Actuators, B*, 2025, **422**, 136631.
- 31 F. Mondaca, *et al.*, Photoluminescence properties of SnO<sub>2</sub> nanoparticles doped with group VI elements (Cr, Mo, W) synthesized by pulsed laser ablation in liquid, *Phys. B*, 2025, **696**, 416625.
- 32 R. Anburaja and S. Kaleemulla, Structural, Magnetic, and Dielectric Properties of Bi<sub>1-x</sub>Co<sub>x</sub>FeO<sub>3</sub> Nanoparticles for Photocatalytic Application, *Braz. J. Phys.*, 2025, **55**(2), 1–14.
- 33 L.-Y. Chen, *et al.*, A review: strategies for reducing the open-circuit voltage loss of wide-bandgap perovskite solar cells, *Chem. Commun.*, 2025, **61**, 1063–1086.
- 34 R. K. Dharman, A. Mariappan and T. H. Oh, Engineering bandgap energy of MoO<sub>3</sub> nanorod heterostructure using AgVO<sub>3</sub> for efficient photocatalytic degradation of antibiotic pollutant, *Environ. Res.*, 2025, **268**, 120829.
- 35 V. Kumar and J. K. Singh, Model for calculating the refractive index of different materials, *Indian J. Pure Appl. Phys.*, 2010, **48**, 571–574.
- 36 C. Fei Guo, *et al.*, Metallic nanostructures for light trapping in energy-harvesting devices, *Light: Sci. Appl.*, 2014, **3**(4), e161.
- 37 P. Cheng, *et al.*, New nanophotonics approaches for enhancing the efficiency and stability of perovskite solar cells, *Adv. Mater.*, 2024, **36**(17), 2309459.
- 38 H. Cheng, *et al.*, Understanding and minimizing non-radiative recombination losses in perovskite light-emitting diodes, *J. Mater. Chem. C*, 2022, **10**(37), 13590–13610.
- 39 R. Sojati, *Solvent Annealing as a Post-treatment: towards Single Crystalline Epitaxial MAPbI<sub>3</sub>*, University of Twente, 2023.
- 40 C.-H. Yeh, *et al.*, Collective Motion of Methylammonium Cations Affects Phase Transition and Self-Trapped Exciton Emission in MAPbI<sub>3</sub> Films, 2024.
- 41 A. F. Castro-Méndez, J. Hidalgo and J. P. Correa-Baena, The role of grain boundaries in perovskite solar cells, *Adv. Energy Mater.*, 2019, **9**(38), 1901489.



- 42 S. Saranya, *et al.*, Nickel-Manganese bimetallic Selenide as an electrode for supercapacitor applications, *Sustain. Energy Technol. Assessments*, 2023, **59**, 103376.
- 43 X. Guo, *et al.*, Non-coordinating charge transfer enables ultrafast desolvation of hydrated zinc ions in the outer Helmholtz layer for stable aqueous Zn metal batteries, *Natl. Sci. Rev.*, 2025, **12**(4), nwaf070.
- 44 Y. Hu, S. Zhao and L. Chen, Prediction of Ruddlesden-Popper antiperovskites K4OBr2 and K4OI2 for potential thermoelectric application, *J. Phys. Chem. C*, 2025, **129**(9), 4656–4663.
- 45 R.-M. Hao, *et al.*, Strong absorption of silica over full solar spectrum boosted by interfacial junctions and light-heat-storage of Mg (OH) 2-(CrOx-SiO2), *Chem. Eng. J.*, 2024, **497**, 154979.
- 46 D. Kaura and S. Bansalb, 2D Magnetic Systems Magnetic Properties, *Fundamentals of Low Dimensional Magnets*, 2022, pp. 73–89.
- 47 L. Fu, *et al.*, Defect passivation strategies in perovskites for an enhanced photovoltaic performance, *Energy Environ. Sci.*, 2020, **13**(11), 4017–4056.
- 48 N. Ahmadvand, E. Mohammadi-Manesh and F. Divakan, Investigating the effect and structural properties of Graphene and Borophene on lead-free perovskite: Introducing the Graphene/CsSnCl3/Borophene, *Mater. Sci. Eng., B*, 2025, **316**, 118138.
- 49 X. Zheng, *et al.*, Boron doping of multiwalled carbon nanotubes significantly enhances hole extraction in carbon-based perovskite solar cells, *Nano Lett.*, 2017, **17**(4), 2496–2505.
- 50 J. Kniepert, *et al.*, Reliability of charge carrier recombination data determined with charge extraction methods, *J. Appl. Phys.*, 2019, **126**(20), 205501.
- 51 F. Gao, *et al.*, Enhancing efficiency of MAPbI3 perovskite solar cells with carbon quantum dot implanted g-C3N4: Controllable crystallization and surface passivation, *J. Alloys Compd.*, 2025, **1017**, 179119.
- 52 I. Zarazua, *et al.*, Surface recombination and collection efficiency in perovskite solar cells from impedance analysis, *J. Phys. Chem. Lett.*, 2016, **7**(24), 5105–5113.
- 53 E. Fabbretti, *et al.*, Enhancing the stability of inverted perovskite solar cells through Cu 2 ZnSnS 4 nanoparticles hole transporting material, *Sustain. Energy Fuels*, 2025, **9**, 1486–1497.

